Electronic Supplementary Material (ESI) for Energy & Environmental Science.

Supporting Information

Enhanced proton and electron reservoir abilities of polyoxometalate grafted on graphene for high-performance hydrogen evolution

Rongji Liu,[a] Guangjin Zhang,*[a] Hongbin Cao,[a] Suojiang Zhang,[a] Yongbin Xie,[a] Ali Haider,[b] Ulrich Kortz,*[b] Banghao Chen,[c] Naresh S. Dalal,*[c] Yongsheng Zhao,[d] Linjie Zhi,[e] Cai-Xia Wu,[f] Li-Kai Yan,*[f] Zhongmin Su[f] and Bineta Keita[g]

[a]Key Laboratory of Green Process and Engineering, Institute of Process Engineering, Chinese Academy of Sciences, 100190, Beijing, China

E-mail: zhanggj@ ipe.ac.cn

[b]Jacobs University, Department of Life Sciences and Chemistry, P.O. Box 750 561, 28725 Bremen, Germany

E-mail: u.kortz@jacobs-university.de

[c]Florida State University, Department of Chemistry and Biochemistry, Tallahassee, FL 32306-4390, USA

E-mail: dalal@chem.fsu.edu

[d]Beijing National Laboratory for Molecular Sciences (BNLMS), Key Laboratory of Photochemistry, Institute of Chemistry, Chinese Academy of Sciences, 100190, Beijing, China

[e]Key Laboratory of Nanosystem and Hierarchical Fabrication, National Center for Nanoscience and Technology, 100190, Beijing, China

[f]Faculty of Chemistry, Northeast Normal University, 130024, Changchun, China

E-mail: yanlk924@nenu.edu.cn

[g]Retired from Université Paris-Sud, Laboratoire de Chimie-Physique, UMR 8000 CNRS, Orsay, F-91405, France.

Table of contents *Page*

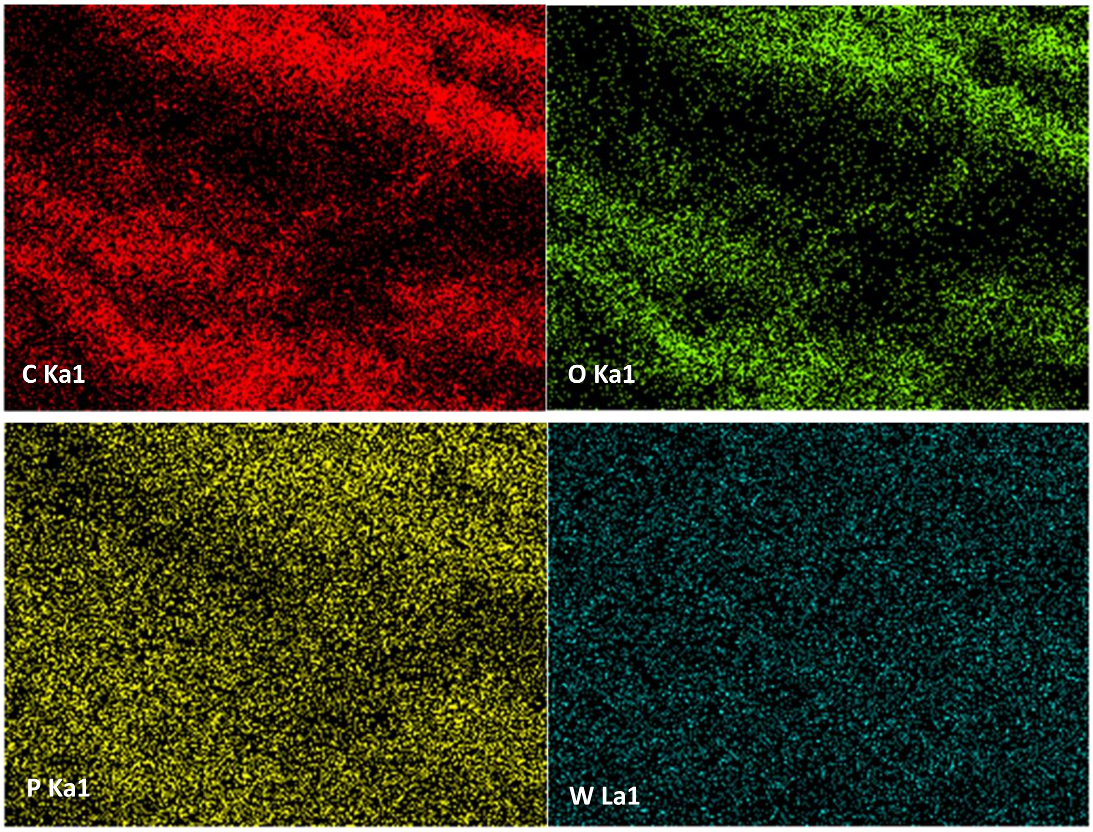

Fig. S1 EDS mapping of **P_8W_{48}/rGO** nanocomposite prepared by electrochemical reduction.

SI-1: X-ray photoelectron spectroscopy (XPS) analysis

Fig. S2a and Fig. S2b show the C 1 *s* XPS spectra of **GO** and **P_8W_{48}/rGO**. It can be clearly seen that the content of C–O group (integration of C-OH and C-O-C) decreases from initial 48.9% of **GO** to 29.5% (shown in Table S1) of **P_8W_{48}/rGO**, indicating that the electrochemical reduction can effectively decrease the amount of oxygen containing groups on **GO**. Meanwhile, the content of graphite-like C (integration of C–C and C=C) group increased from initial 42% to 63.3%, indicating that significant sp^3/sp^2 -hybridized carbon structures were restored. The W (4*f*) and P (2*p*) XPS spectras of **P_8W_{48}/rGO** were also shown in Fig. S2. The W 4$f_{7/2}$ and W 4$f_{5/2}$ doublets with binding energies of 35.48 and 37.62 eV (Fig. S2c) respectively for **P_8W_{48}/rGO** indicate that tungsten is in its full oxidation form (W^{VI}) in **P_8W_{48}**, which is in line with that of precursor **P_8W_{48}** (Fig. S2e). It should be noted that there are broad peaks at the binding energy higher than 40 eV for both **P_8W_{48}** and **P_8W_{48}/rGO**, which can be assigned to W^{VI} loss features. The presence of phosphorus with strong signal was also detected in the **P_8W_{48}/rGO** composite as shown in Fig. S2d, even though it has low content in P_8W_{48} (the P 2*p* of **P_8W_{48}** was also shown in Fig. S2f), which indicates the intensive adsorption of P_8W_{48} on **rGO**. However, it is worth noting that the W^{VI}

4*f* peaks of the **P_8W_{48}/rGO** nanocomposite shift to lower binding energies compared with those of **P_8W_{48}** (Table S2), which suggests the electron transfer from **P_8W_{48}** to **rGO** decreasing the electronegativity of the adjacent terminal oxygen atoms of **P_8W_{48}**.[1] On the other hand, the atomic ratios of P/W for both **P_8W_{48}** and **P_8W_{48}/rGO** are almost the same, which suggest the intact **P_8W_{48}** is still there in the **P_8W_{48}/rGO** nanocomposite. However, it is well known that XPS is not appropriate for quantitative determination of atomic percentage.

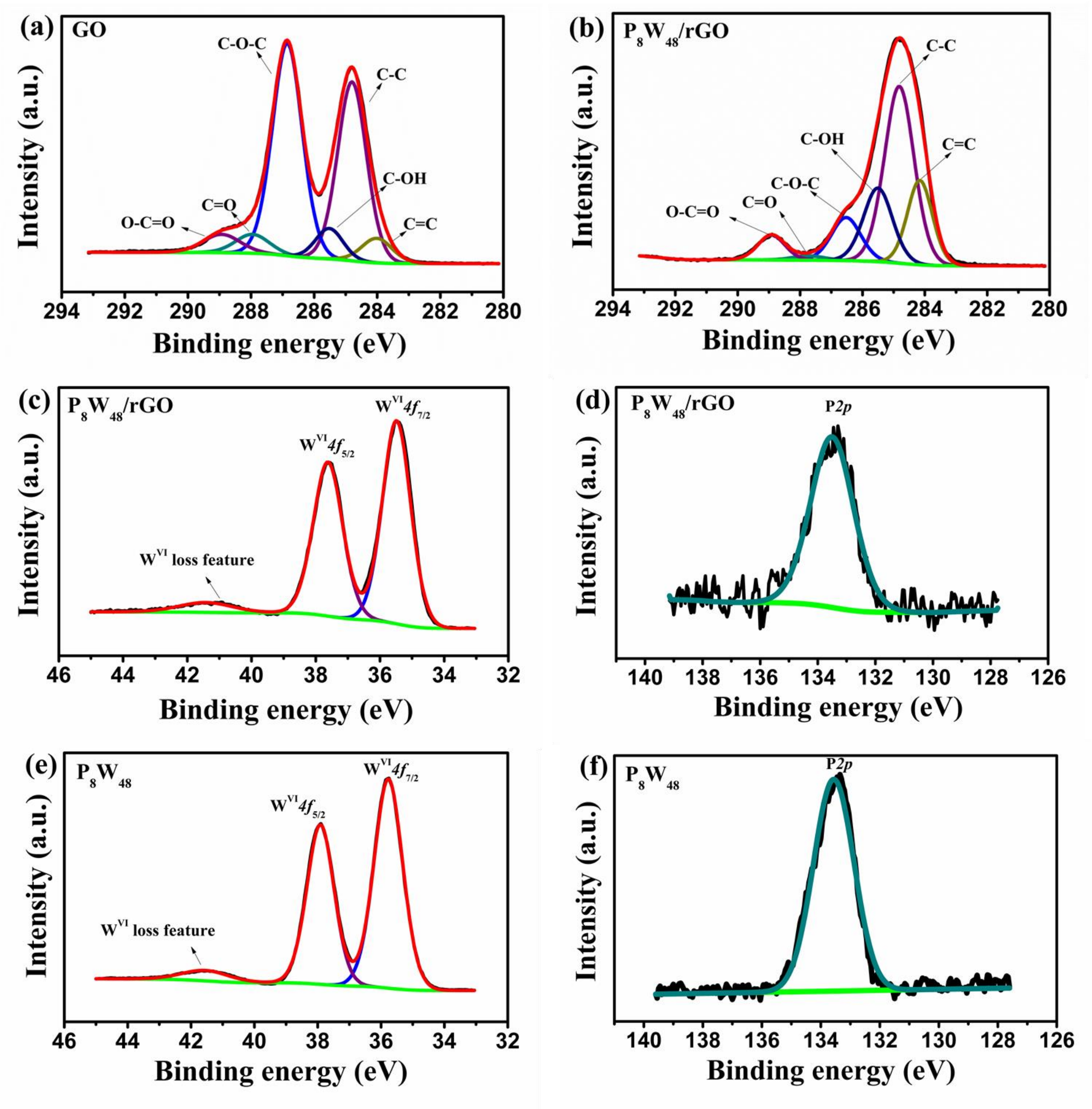

Fig. S2 (a) C *1s* XPS spectrum of **GO**. (b**)** C *1s*, (c**)** W^{VI} *4f* and (d) P *2p* XPS spectra of the as-prepared **P_8W_{48}/rGO** nanocomposite. (e) W^{VI} *4f* and (f) P *2p* XPS spectra of **P_8W_{48}**.

Table S1 Fitting of the C 1*s* peak binding energy (eV) (relative atomic percentage %)

Samples	graphite-like C		C-O		C=O	O-C=O
	C-C	C=C	C-OH	C-O-C		
GO	284.8 [36.8%]	284.0 [5.2%]	285.5 [5.6%]	286.9 [43.3%]	288.0 [4.3%]	288.9 [4.8%]
P_8W_{48}/rGO	284.8 [45.2%]	284.2 [18.1%]	285.5 [18.6%]	286.5 [10.9%]	287.8 [1.4%]	288.9 [5.8%]
P_8W_{48}/rGO-25	284.8 [40.8%]	284.0 [1.6%]	285.7 [11.4%]	286.9 [35.9%]	287.9 [6.5%]	289.0 [3.8%]
P_8W_{48}/rGO-50	284.8 [41.7%]	284.2 [5.0%]	285.8 [16.3%]	287.0 [27.1%]	287.7 [5.4%]	288.9 [4.5%]

Table S2 The binding energies (BE) of P *2p* and W *4f* and the atomic ratio of P/W for **P_8W_{48}**, **P_8W_{48}/rGO**, **P_8W_{48}/rGO-25** and **P_8W_{48}/rGO-50** respectively

Samples	BE (P *2p*)	BE (W *4f* $_{7/2}$)	BE (W *4f* $_{5/2}$)	P/W (At. %/ At. %)
P_8W_{48}	133.54	35.77	37.91	0.229
P_8W_{48}/rGO	133.50	35.48	37.62	0.227
P_8W_{48}/rGO-25	133.42	35.58	37.72	0.311
P_8W_{48}/rGO-50	133.51	35.70	37.80	0.315

SI-2: Raman spectroscopy analysis

Raman spectroscopy can provide additional information for probing defects and structural properties of carbon materials. As shown in Fig. S3, two fundamental vibrations which are attributed to the D (~1350 cm^{-1}) and G (~1595 cm^{-1}) bands, respectively, are observed for both **GO** and **P_8W_{48}/rGO**. The D band is a breathing mode or k-point photons of A_{1g} symmetry originating from the disorder-induced mode associated with structural defects and imperfections and the G band corresponds to the first-order scattering of the E_{2g} mode from the sp^2 carbon domains.[2,3] The intensity ratio of D and G bands, I_D/I_G, can be used for the determination of disorder degree and average size of the sp^2 domains. It can be observed that the I_D/I_G intensity ratio of **P_8W_{48}/rGO** (1.30) is higher than that of **GO** (0.92), indicating a decrease in the average size of the sp^2 domains upon reduction of exfoliated **GO**, and it can be explained if new graphitic domains were created that are smaller in size than those present in **GO** before reduction, but more abundant in number.[4]

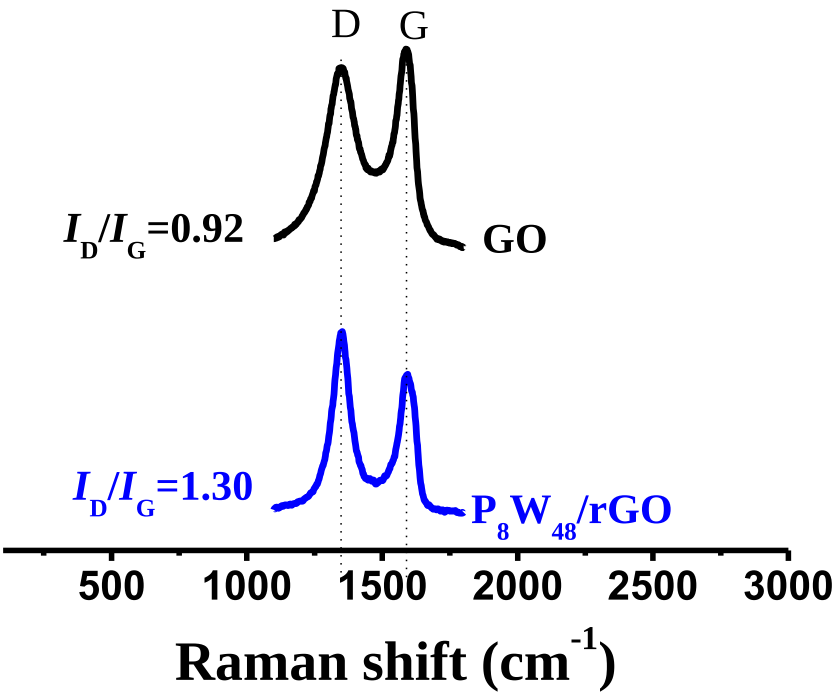

Fig. S3 Raman spectra of **GO** and **P_8W_{48}/rGO** nanocomposite.

SI-3: Fourier transform infrared spectroscopy (FT-IR) analysis

FT-IR spectra were recorded to further confirm the structural integrity of **P_8W_{48}** in the **P_8W_{48}/rGO** nanocomposite. Figure S4 shows the FT-IR spectra of **GO**, **rGO**, **P_8W_{48}** and **P_8W_{48}/rGO** nanocomposite. It can be clearly observed that the Hummer's **GO** has the characteristic signals of −OH group, C=O symmetry vibration peaks, C=C sp^2 species and C−O vibration peaks. When the **GO** reduction reaction occurred, no stretching vibration of carboxyl groups was observed in the spectra of both **rGO** and **P_8W_{48}/rGO**, confirming the efficient reduction of **GO** to **rGO**.[6,10b] It should be noted that the C−O vibration peaks and hydroxyl groups are still remained in the **rGO**, which facilitates its interaction with **P_8W_{48}**; the C−O vibration peaks in the spectra of **rGO** are merged with the POM bands (vibration bands of ν_{as} P–O) in that of **P_8W_{48}/rGO**. On the other hand, the POM bands for the free **P_8W_{48}** are at 1140 cm^{-1} and 1084 cm^{-1} (ν_{as} P–O),[1] 1015 cm^{-1} (ν_{as} W=O_t), 924 cm^{-1} (ν_{as} W–O_b–W), and 807 cm^{-1} (ν_{as} W–O_c–W). Whereas for the **P_8W_{48}/rGO** nanocomposite, all corresponding bands are shifted by several wavenumbers and identified at 1140 cm^{-1} and 1100 cm^{-1} for ν_{as} P–O, 1034 cm^{-1} for ν_{as} W=O_t, 904 cm^{-1} for ν_{as} W–O_b–W, and 820 cm^{-1} for ν_{as} W–O_c–W, although some peaks are weak due to the low concentrations of **P_8W_{48}** on **rGO**. Altogether, these results suggest a strong interaction between the **rGO** sheets and the grafted, intact **P_8W_{48}** nanoclusters, which is in agreement with the XPS observations.

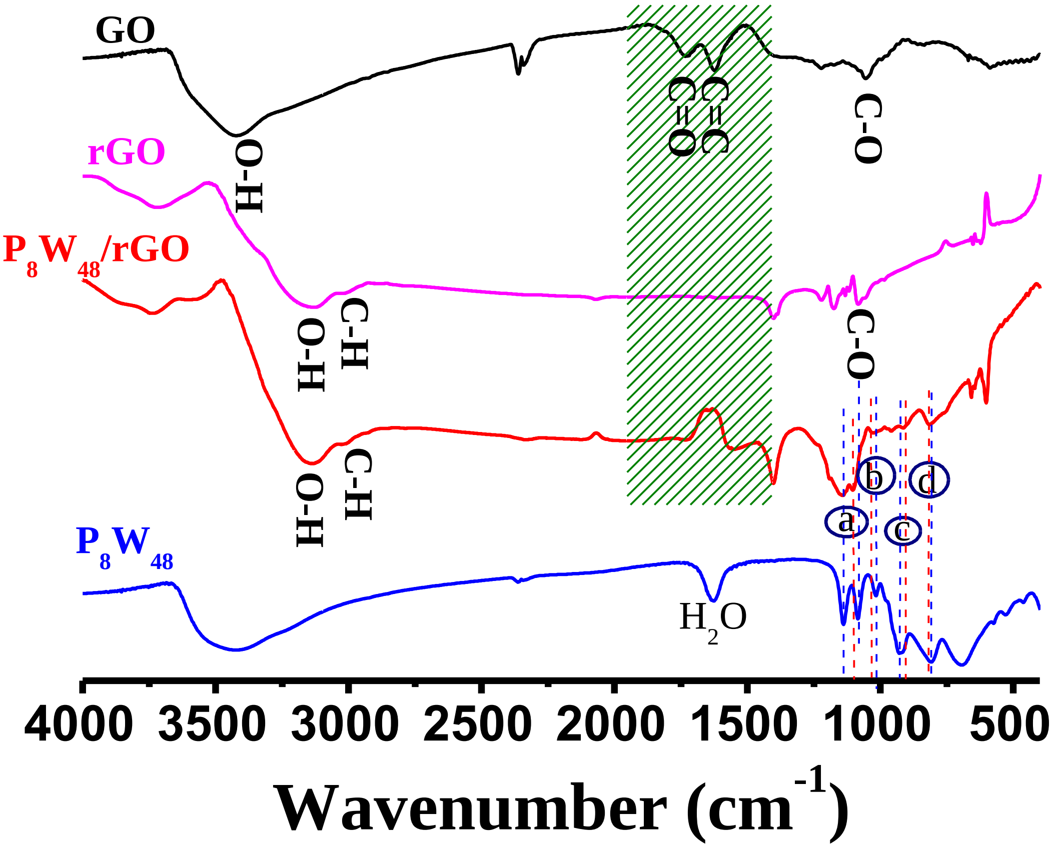

Fig. S4 FT-IR spectra of **GO**, **rGO**, **P_8W_{48}** and **P_8W_{48}/rGO** nanocomposite. The shaded region from ~1400 to 1900 cm^{-1} includes the signal of the C=C sp^2 species and carboxylic groups. The peak observed at ~1600 cm^{-1} in the spectra of **P_8W_{48}** is due to the hydration water molecules. Notes: *a* ν_{as} P–O, *b* ν_{as} W=O_t, *c* ν_{as} W–O_b–W, *d* ν_{as} W–O_c–W.

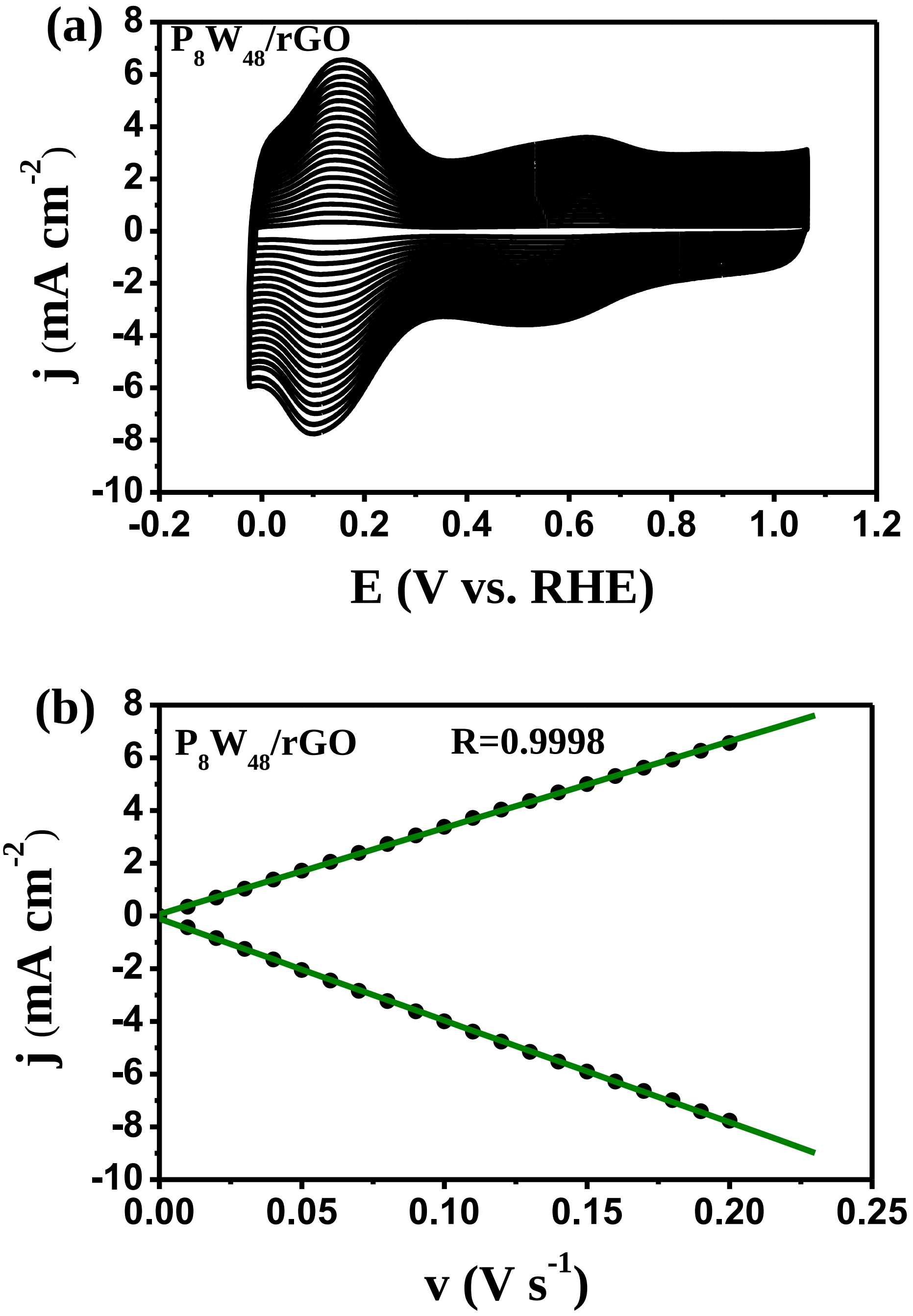

Fig. S5 (a) Cyclic voltammograms and peak current intensity variations for **P_8W_{48}/rGO** in a 0.5 M H_2SO_4 (pH 0.3) medium in the potential domain from 1.065 V to ~ (-0.025) V vs. RHE. The cyclic voltammograms are shown as a function of scan rate (from inner to outer curve: 10, 20, 30, 40, 50, 60, 70, 80, 90, 100, 110, 120, 130, 140, 150, 160, 170, 180, 190 and 200 mV s^{-1}, respectively). (b) Dependence of cathodic and anodic peak currents of the first W wave as a function of the scan rate.

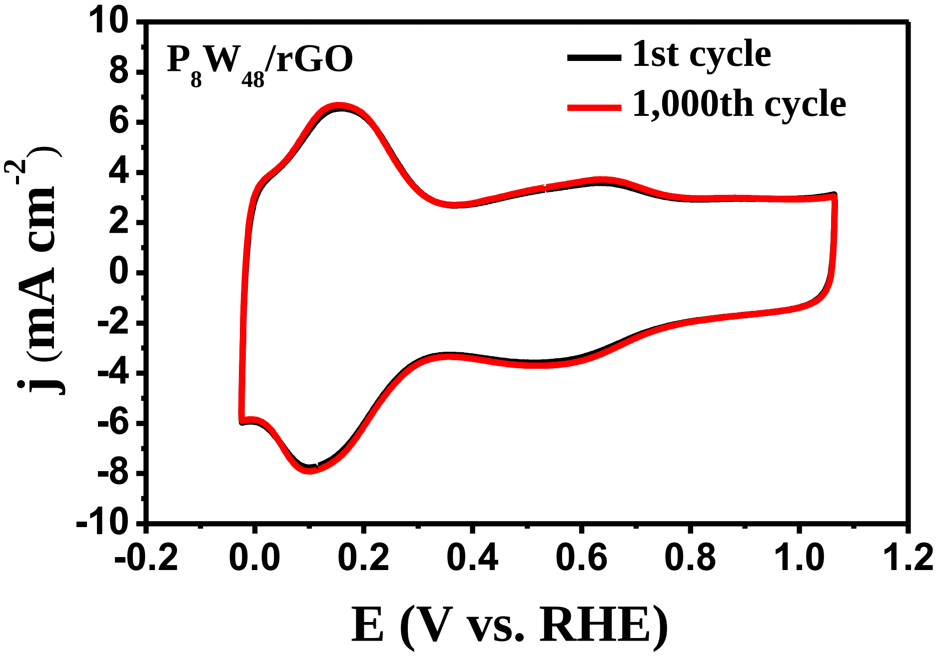

Fig. S6 Comparison of the cyclic voltammograms recorded with **P_8W_{48}/rGO** before and after 1,000 cycles in a 0.5 M H_2SO_4 (pH=0.3) medium. The scan rate was 200 mV s^{-1}.

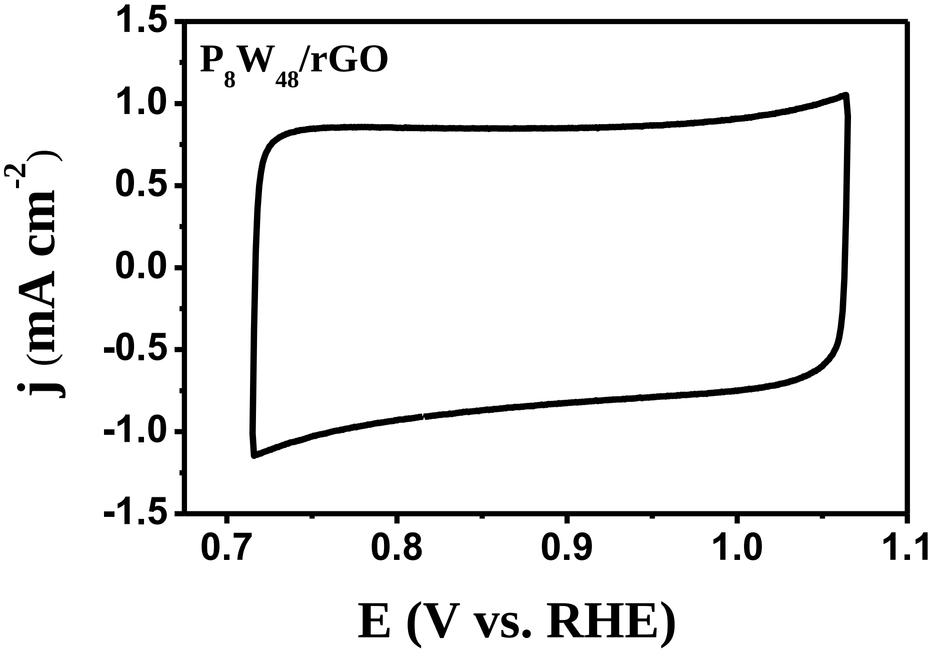

Fig. S7 Cyclic voltammogram recorded with **P_8W_{48}/rGO** in a 0.5 M H_2SO_4 (pH=0.3) medium in the potential domain from 1.065 V to 0.715 V vs. RHE. The scan rate was 100 mV s^{-1}.

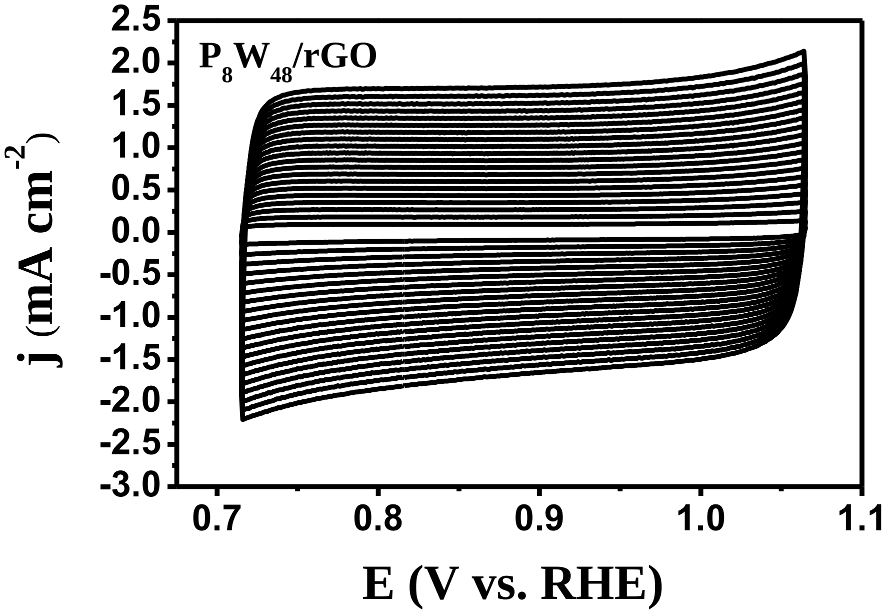

Fig. S8 Cyclic voltammograms and current intensity variations for **P_8W_{48}/rGO** in a 0.5 M H_2SO_4 (pH 0.3) medium in the potential domain from 1.065 V to 0.715 V vs. RHE. The cyclic voltammograms are shown as a function of scan rate (from inner to outer curve: 10, 20, 30, 40, 50, 60, 70, 80, 90, 100, 110, 120, 130, 140, 150, 160, 170, 180, 190 and 200 mV s^{-1}, respectively).

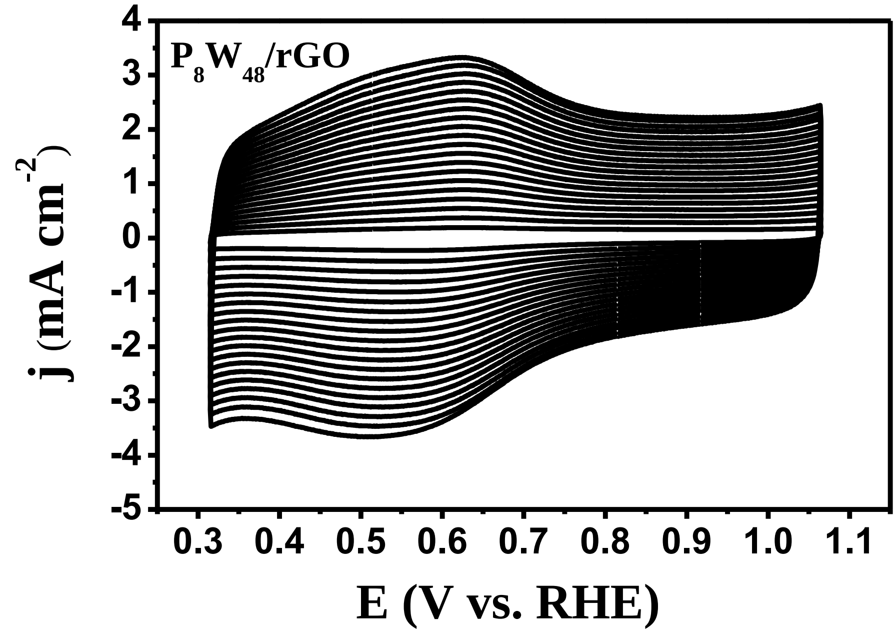

Fig. S9 Cyclic voltammograms and peak current intensity variations for **P_8W_{48}/rGO** in a 0.5 M H_2SO_4 (pH 0.3) medium in the potential domain from 1.065 V to ~0.315 V vs. RHE. The cyclic voltammograms are shown as a function of scan rate (from inner to outer curve: 10, 20, 30, 40, 50, 60, 70, 80, 90, 100, 110, 120, 130, 140, 150, 160, 170, 180, 190 and 200 mV s^{-1}, respectively).

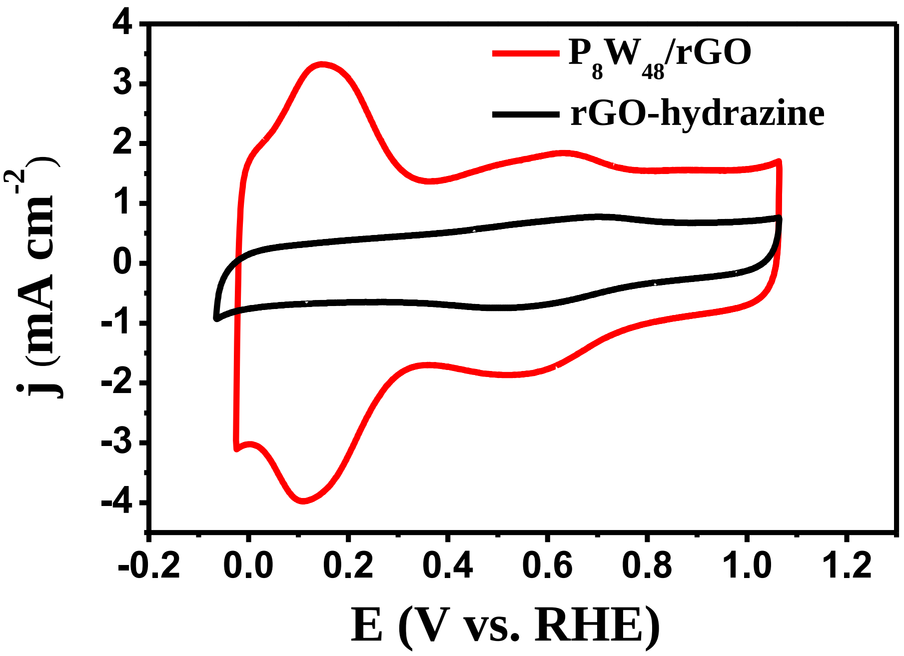

Fig. S10 Superimposed representative cyclic voltammograms of **P_8W_{48}/rGO** and **rGO-hydrazine** recorded in a 0.5 M H_2SO_4 (pH 0.3) medium at a scan rate of 100 mV s^{-1}.

SI-4: Pt deposition

When Pt is used as the counter electrode, and there are chlorides inpurities in the electrolyte, Pt counter electrode dissolution will happen and thus the Pt deposition on the working electrode, which will increase the HER current and will make wrong estimation of the real catalytic activities of the catalysts. In order to ascertain this, protocols are as follows. A standard three-electrode cell was used and was controlled at 25 ^{o}C using a water bath during the experiment. The prepared P_8W_{48}/rGO modified GC RDE (4 mm in diameter) was used as the working electrode. A Pt gauze and a SCE were used as counter and reference electrodes, respectively. The electrolyte, 0.5 M H_2SO_4 (pH=0.3), was saturated with ultrahigh-purity Ar for at least 30 min and kept under a positive pressure of this gas during the experiments. To speed up the anodic dissolution of Pt in acidic media, the Pt counter electrode and the working electrode were placed in the same compartment, and the reference electrode was separated by a glass frit. For Pt deposition, 5 mM HCl was added to the electrolyte, and then continuous potential cycling (1758 cycles) was performed in the potential domain from +1.065 to -0.05 V vs. RHE at a scan rate of 50 mV s^{-1}. As the cycling goes, the characteristics of the HER wave is evolved and improved gradually. Fig. S11a shows that the CV of the resulting tricomponent **Pt-P_8W_{48}/rGO** exhibits an additional oxidation wave at + 0.02 V compared to that of **P_8W_{48}/rGO**, along with the apparent HER wave. This oxidation wave is attributed to hydrogen oxidation as featured at the same location on the **Pt/C** CV (Fig. S11b).

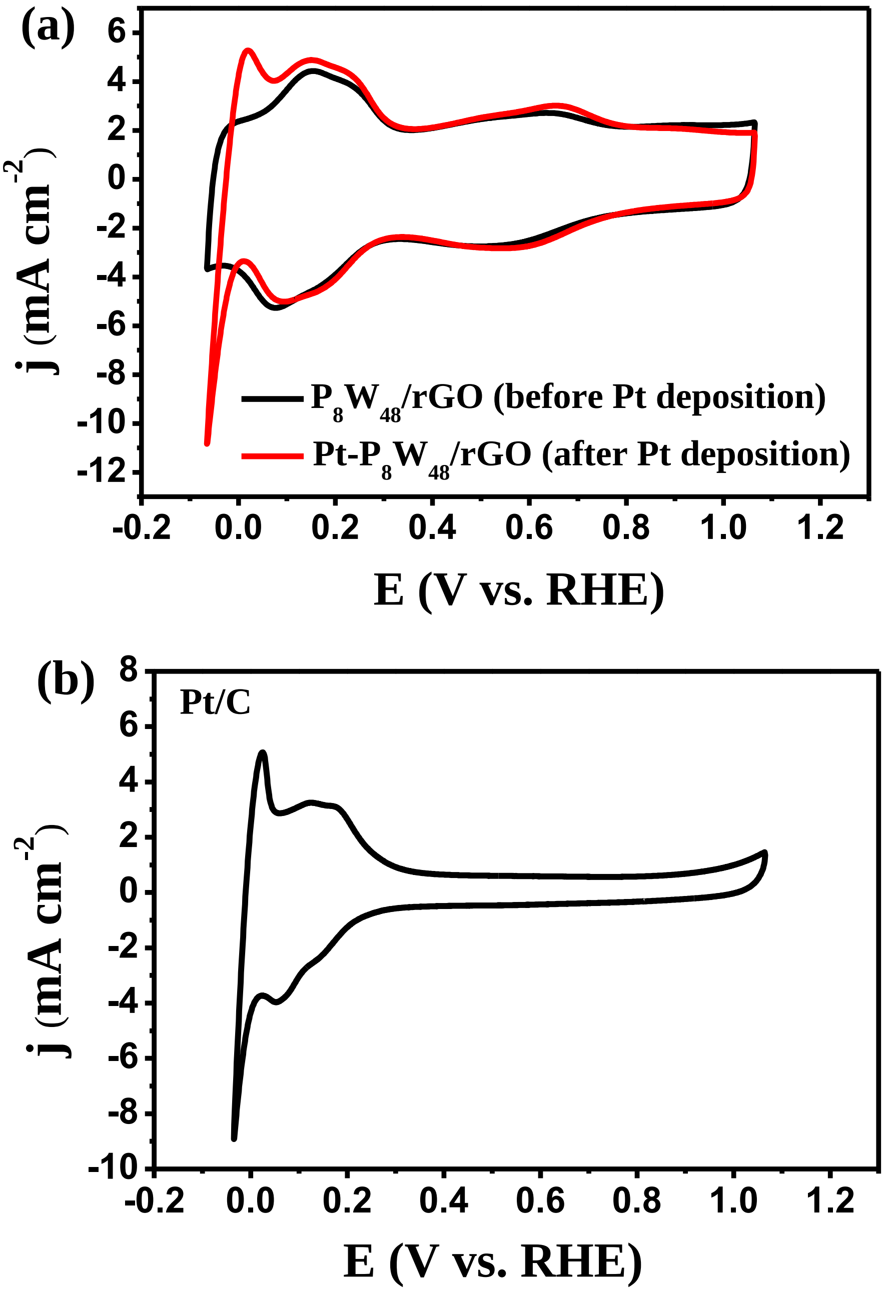

Fig. S11 (a) Comparison of representative cyclic voltammograms of **P_8W_{48}/rGO** and **Pt- P_8W_{48}/rGO** after Pt deposition. (b) Cyclic voltammograms of **Pt/C**. The catalyst loading was 0.3 mg cm^{-2}. The scan rate was 100 mV s^{-1}.

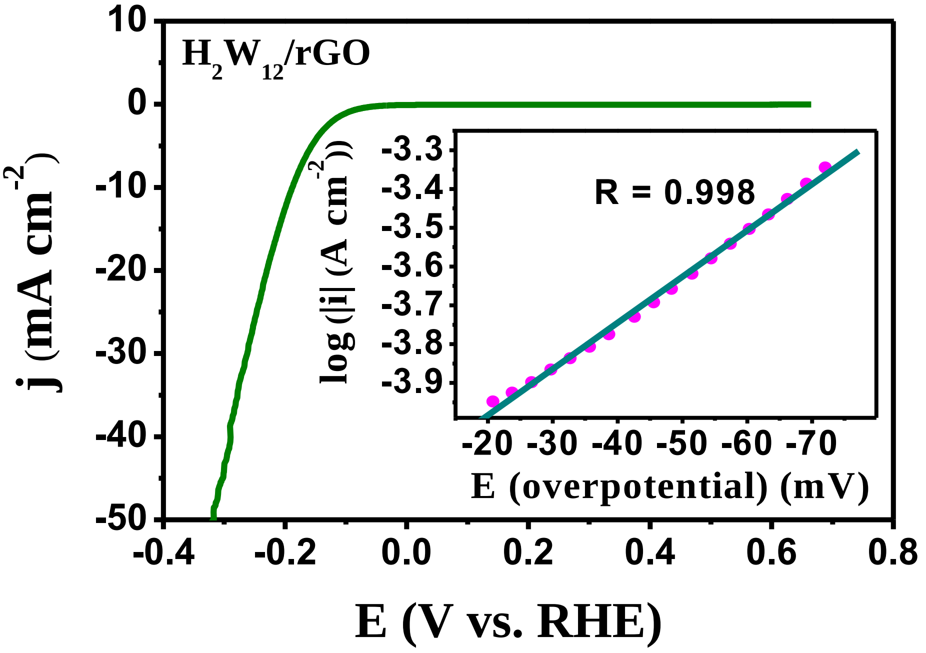

Fig. S12 Polarization curve obtained with **H_2W_{12}/rGO** recorded on glassy carbon electrode, the inset is the corresponding Tafel plot obtained from the LSV curve.

Table S3 Comparison of HER activity measured for **P_8W_{48}/rGO** with that reported for other systems with known HER activity under acidic conditions.

catalyst	Loading (mg cm^{-2})	Electrode	Electrolyte	J^a (mA cm^{-2})	η^b (mV vs. RHE)	J$_0$^{c} (A cm^{-2})	Tafel slope (mV dec^{-1})	TOF (s^{-1})	Ref.
P_8W_{48}/rGO	0.3	Glassy carbon	0.5M H_2SO_4	10	28	2×10^{-3}	38	1.4 (195)^d	This work
				20	39			4.5 (245)^d	
				50	70			11.3 (295)^d	
rGO-hydrazine	0.3	Glassy carbon	0.5M H_2SO_4	1	~180	1.14×10^{-5}	84	N/A	This work
H_2W_{12}/rGO	0.3	Glassy carbon	0.5M H_2SO_4	10	~188	6×10^{-5}	84	N/A	This work
$Co_{0.6}Mo_{1.4}N_2$	0.243	Glassy carbon	0.1M HClO4	10	~190	2.3×10^{-4}	N/A	N/A	5
Ni_2P	1	Ti foil	0.5M H_2SO_4	20	130	4.91×10^{-4}	46	0.015 (100)^d 0.5 (200)^d	6
2H-MoS_2 film	N/A	Glassy carbon	0.5M H_2SO_4	1	300	2.4×10^{-6}	86	0.013 (0)^d	7
MoS_2/ MoO_3	N/A	FTO	0.5M H_2SO_4	2	200	N/A	50-60	4 (272)^d	8

1T-Li_xMoS_2	N/A	Graphitic rod	0.5M H_2SO_4	10	185	N/A	43	N/A	9
Bulk Mo_2C	3.3	Carbon paste electrode	0.5M H_2SO_4	20	~225	1.3×10^{-6}	56	N/A	10
Bulk MoB	2		0.5M H_2SO_4	20	~225	1.4×10^{-6}	55	N/A	
Mo_2C/CNT	2	Carbon paper	0.1M $HClO_4$	10	~150	1.4×10^{-5}	55.2	N/A	11
NiMoNx/C	0.25	Glassy carbon	0.1M $HClO_4$	3.5	~200	2.4×10^{-4}	35.9	N/A	12
Ni-Mo	3	Ti foil	0.5M H_2SO_4	20	80	N/A	N/A	0.05 (100) ^{d} 0.36 (200)^{d}	13
MoS_2/rGO	0.28	Glassy carbon	0.5M H_2SO_4	10	~150	N/A	41	N/A	14
POMOFs	0.1	Carbon paste electrode	1 M LiCl + HCl (pH 1)	NA	NA	N/A	N/A	6.7 (200)^{d}	15
$(PEI/P_5W_{30}\text{-rGO})_n$	N/A	Glassy carbon	0.05M H_2SO_4	1.7	550	N/A	N/A	N/A	16
Hex-WO_3 by MH	N/A	Glassy carbon	1 M H_2SO_4	5.81	0	6.61×10^{-3}	116	N/A	17
				33.67	100				
				75.80	200				
WS_2 nanoflake	0.35	Glassy carbon	0.5 M H_2SO_4	10	~150	N/A	48	N/A	18
1T-WS_2 nanosheets	1.0±0.2	graphite disk	0.5 M H_2SO_4	10	142	N/A	70	N/A	19
CoS_2/rGO-CNT	1.15 for CoS_2	3D structure of the film	0.5 M H_2SO_4	10	142	6.3×10^{-5}	51	N/A	20
				20	153				
				100	178				
$Ni_{12}P_5$	3	Ti foil	0.5 M H_2SO_4	10	107	N/A	63	0.019 (120)^{d}	21
				20	141				
				40	190				
CoP	2	Ti foil	0.5 M H_2SO_4	20	85	1.4×10^{-4}	50	0.0047 (20)^{e}	22
CoP	0.92	carbon cloth	0.5 M H_2SO_4	10	67	2.88×10^{-4}	51	4 (240, pH=0)^{d}	23
				20	100				
				100	204				
CoS_2 NW	1.7 ±0.3	graphite	0.5 M H_2SO_4	10	145	1.51×10^{-5}	51.6	N/A	24
$W(S_{0.48}Se_{0.52})_2$	0.21	Carbon cloth	1 M H_2SO_4	100	360	2.9×10^{-5}	105	N/A	25
MoS_2/rGO	0.2	Glassy carbon	0.5 M H_2SO_4	50	235	N/A	41	N/A	26

$CoSe_2$ NP	2.8	Carbon fiber paper	0.5 M H_2SO_4	10	139	$(4.9 \pm 1.4) \times 10^{-6}$	42.1	N/A	27
				100	184				
$[Mo_3S_{13}]^{2-}$ clusters	0.01-0.1	Graphite paper	0.5 M H_2SO_4	10	180-220	N/A	38-40	3 (200)^d	28
MoP | S	3	Ti foil	0.5 M H_2SO_4	10	64	5.7×10^{-4}	50	0.75 (150)^d	29
				20	78				
				100	120				
double-gyroid MoS_2	0.06	FTO	0.5 M H_2SO_4	10	~ 230	6.9×10^{-7}	50	N/A	30
1T WS_2	0.0065	Glassy carbon	0.5 M H_2SO_4	10	~230	2×10^{-5}	60	175 (288)^d	31
cGO/MoS_x	N/A	Carbon cloth	0.5 M H_2SO_4	220	300	N/A	51.9	N/A	32
NENU-500	~0.38	Glassy carbon	0.5 M H_2SO_4	10	237	$3.6 \text{x} 10^{-5}$	96	N/A	33

^{a}Current density (mA cm^{-2})

^{b}Overpotential (mV vs. RHE)

^{c}Exchange current density (A cm^{-2})

^{d}The TOF values were obtained at the specified overpotentials (mV vs. RHE)

^{e}The TOF values were obtained at the specified current densities (mA cm^{-2})

$^{N/A}$These values were unavailable

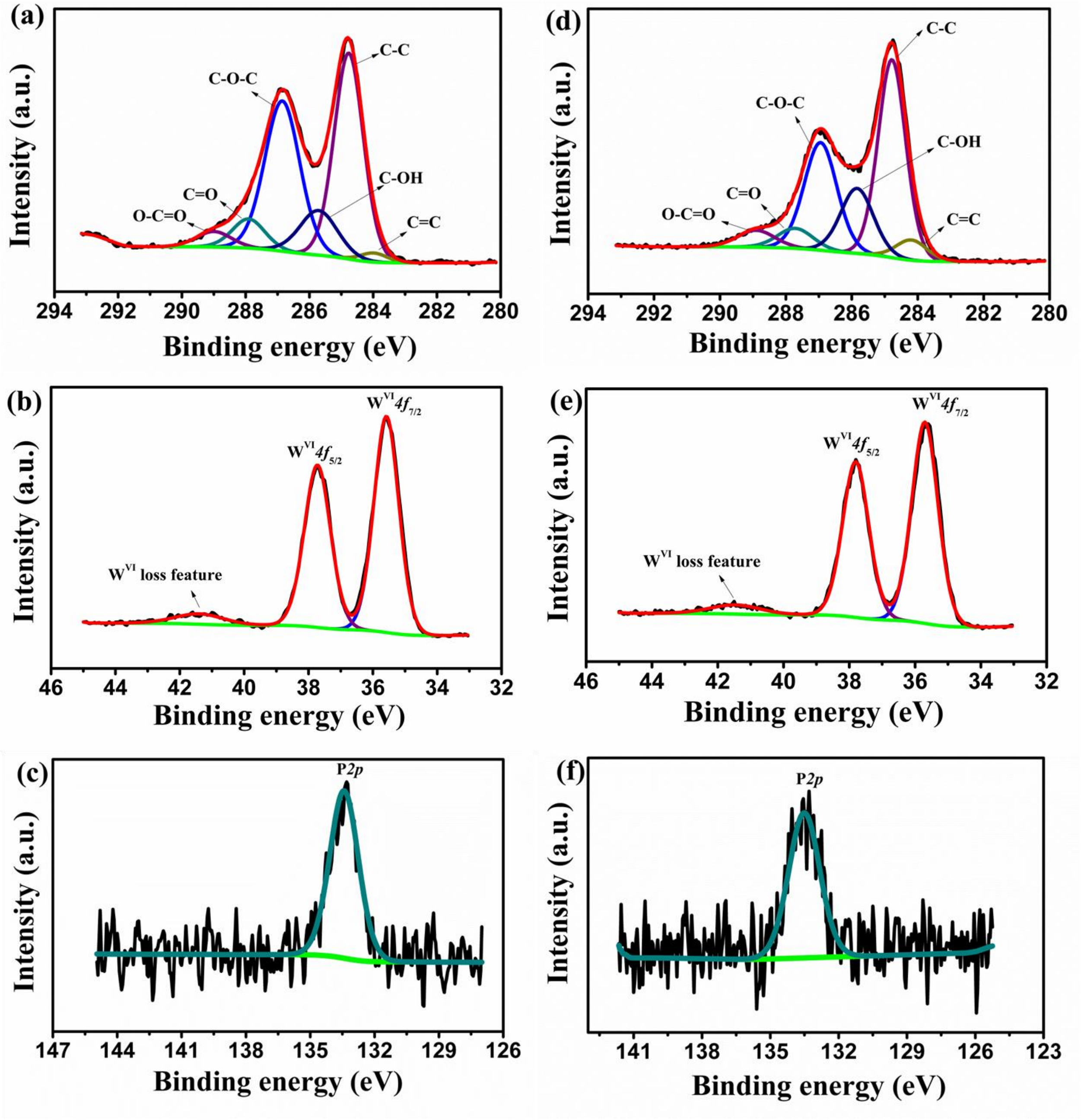

Fig. S13 (a) C *1s*, (b) W^{VI} *4f* and (c) P *2p* XPS spectra of the as-prepared **P_8W_{48}/rGO-25** nanocomposite. (d) C *1s*, (e) W^{VI} *4f* and (f) P *2p* XPS spectra of the as-prepared **P_8W_{48}/rGO-50** nanocomposite.

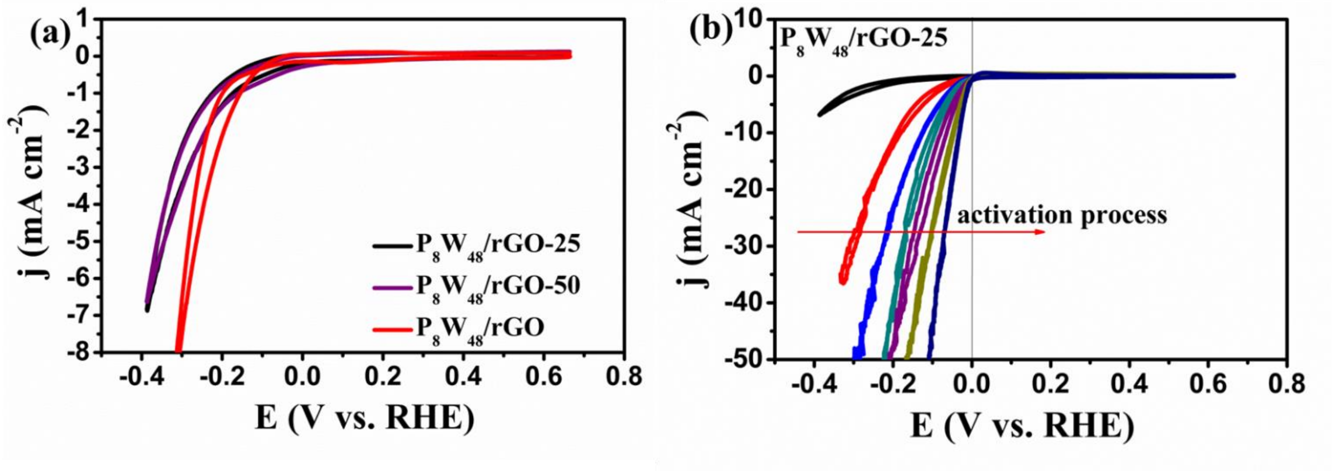

Fig. S14 (a) Influences of reduction degree of GO on the performance of HER (the data was extracted from 10th cycle for each electrode). (b) The variation of the cyclic voltammogram characteristics of P_8W_{48}/rGO-25 during the potential cycling. The catalyst loading was 0.3 mg cm^{-2}. The scan rate was 2 mV s^{-1}.

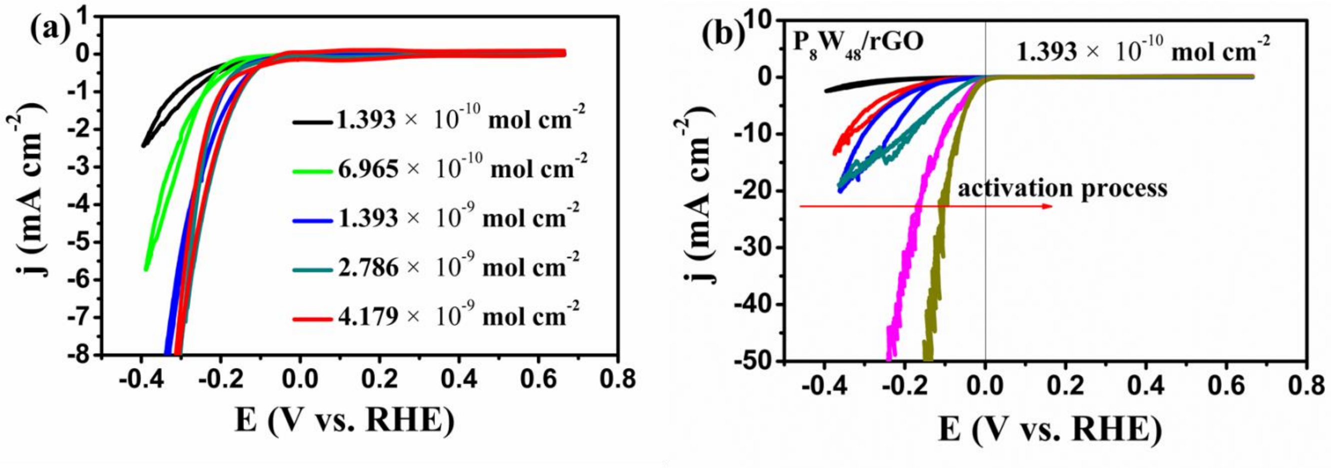

Fig. S15 (a) Influences of the loading amount of $\mathbf{P_8W_{48}}$ on the performance of HER (the data was extracted from 10th cycle for each electrode). (b) The variation of the cyclic voltammogram characteristics of P_8W_{48}/rGO with P_8W_{48} loading of 1.393×10^{-10} mol cm^{-2} during the cycling. The scan rate was 2 mV s^{-1}.

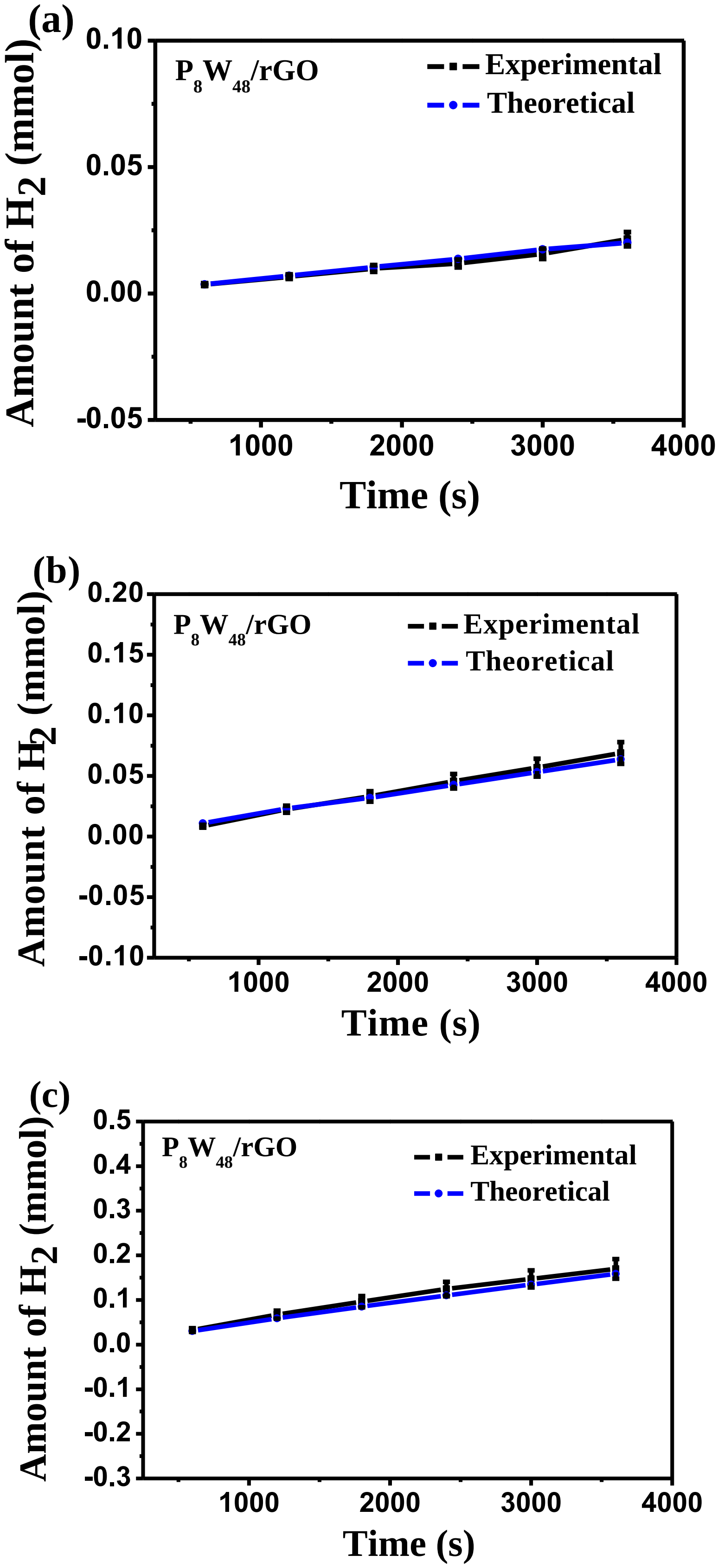

Fig. S16 Faradaic yield (both experimentally measured and theoretically calculated) of H_2 production versus time for **P_8W_{48}/rGO** at different overpotentials of (a) η=195 mV, (b) η=245 mV and (c) η=295 mV for 3600 s in 0.5 M H_2SO_4.

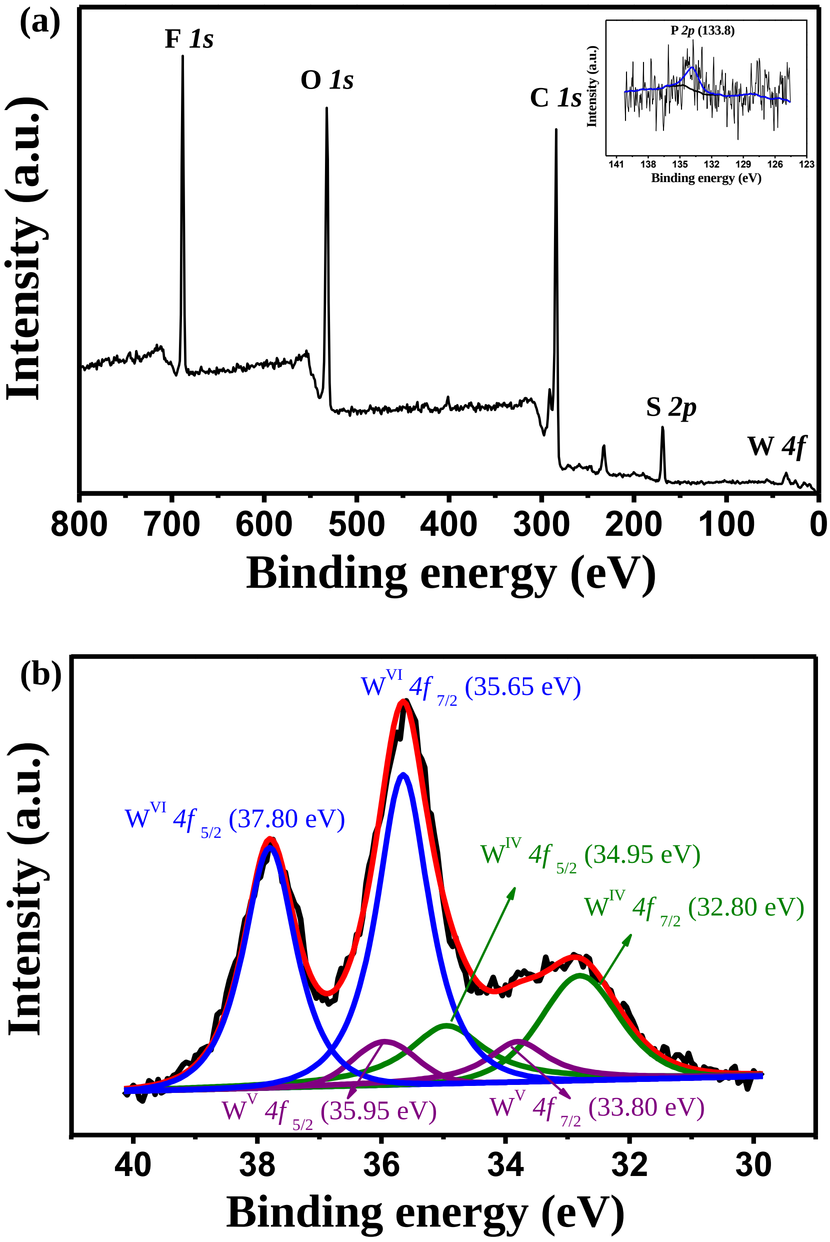

Fig. S17 (a) XPS spectra (survey) and (b) W4*f* XPS spectra recorded from the film (**P_8W_{48}/rGO/Nafion** modified electrode) after activation. Inset of (a) is the corresponding P *2p* XPS spectra.

SI-5: Description of Movie S1

Controlled potential coulometry measurement was performed for the quantitative detection of H_2 production at η=295 mV. Hydrogen evolution occurred rapidly and at a high rate over the **P_8W_{48}/rGO** electrocatalytic film.

References

1. Wang, S., Li, H., Li, S., Liu, F., Wu, D., Feng, X. & Wu, L. Electrochemical-reduction-assisted

assembly of a polyoxometalate/graphene nanocomposite and its enhanced lithium-storage performance. *Chem. Eur. J.* **19**, 10895-10902 (2013).

2. Ferrari, A. C., Meyer, J. C., Scardaci, V. C., Lazzeri, C. M., Mauri, F., Piscanec, S., Jiang, D., Novoselov, K. S., Roth, S. & Geim, A. K. Raman spectrum of graphene and graphene layers. *Phys. Rev. Lett.* **97**, 187401-187404 (2006).
3. Liu, R., Li, S., Zhang, G., Dolbecq, A., Mialane, P. & Keita, B. Polyoxometalate-mediated green synthesis of graphene and metal nanohybrids: high-performance electrocatalysts. *J. Clust. Sci.* **25**, 711–740 (2014).
4. Stankovich, S., Dikin, D. A., Piner, R. D., Kohlhaas, K. A., Kleinhammes, A., Jia, Y., Wu, Y., Nguyen, S. T. & Ruoff, R. S. Synthesis of graphene-based nanosheets via chemical reduction of exfoliated graphite oxide. *Carbon* **45**, 1558-1565 (2007).
5. Cao, B., Veith, G. M., Neuefeind, J. C., Adzic, R. R. & Khalifah, P. G. Mixed close-packed cobalt molybdenum nitrides as non-noble metal electrocatalysts for the hydrogen evolution reaction. *J. Am. Chem. Soc.* **135**, 19186-19192 (2013).
6. Popczun, E. J., McKone, J. R., Read, C. G., Biacchi, A. J., Wiltrout, A. M., Lewis, N. S. & Schaak, R. E. Nanostructured nickel phosphide as an electrocatalyst for the hydrogen evolution reaction. *J. Am. Chem. Soc.* **135**, 9267-9270 (2013).
7. Kong, D., Wang, H., Cha, J. J., Pasta, M., Koski, K. J., Yao, J. & Cui, Y. Synthesis of MoS_2 and $MoSe_2$ films with vertically aligned layers. *Nano Lett.* **13**, 1341-1347 (2013).
8. Chen, Z., Cummins, D., Reinecke, B. N., Clark, E., Sunkara, M. K. & Jaramillo, T. F. Core–shell MoO_3–MoS_2 nanowires for hydrogen evolution: A functional design for electrocatalytic materials. *Nano Lett.* **11**, 4168-4175 (2011).
9. Lukowski, M. A., Daniel, A. S., Meng, F., Forticaux, A., Li, L. & Jin, S. Enhanced hydrogen evolution catalysis from chemically exfoliated metallic MoS_2 nanosheets. *J. Am. Chem. Soc.* **135**, 10274-10277 (2013).
10. Vrubel, H. & Hu, X. Molybdenum boride and carbide catalyze hydrogen evolution in both acidic and basic solutions. *Angew. Chem.* **124**, 12875-12878 (2012).
11. Chen, W., Wang, C., Sasaki, K., Marinkovic, N., Xu, W., Muckerman, J. T., Zhu, Y. & Adzica, R. R. Highly active and durable nanostructured molybdenum carbide electrocatalysts for hydrogen production. *Energy Environ. Sci.* **6**, 943-951 (2013).

12. Chen, W., Sasaki, K., Ma, C., Frenkel, A. I., Marinkovic, N., Muckerman, J. T., Zhu, Y. & Adzic, R. R. Hydrogen-evolution catalysts based on non-noble metal nickel–molybdenum nitride nanosheets. *Angew. Chem. Int. Ed.* **51**, 6131-6135 (2012).
13. McKone, J. R., Sadtler, B. F., Werlang, C. A., Lewis, N. S. & Gray, H. B. Ni−Mo nanopowders for efficient electrochemical hydrogen evolution. *ACS Catal.* **3**, 166-169 (2013).
14. Li, Y., Wang, H., Xie, L., Liang, Y., Hong, G. & Dai, H. MoS_2 nanoparticles grown on graphene: An advanced catalyst for the hydrogen evolution reaction. *J. Am. Chem. Soc.* **133**, 7296-7299 (2011**)**.
15. Nohra, B., El Moll, H., Rodriguez Albelo, L. M., Mialane, P., Marrot, J., Mellot-Draznieks, C., O'Keeffe, M., Ngo Biboum, R., Lemaire, J., Keita, B., Nadjo, L. & Dolbecq, A. Polyoxometalate-based metal organic frameworks (POMOFs): Structural trends, energetics, and high electrocatalytic efficiency for hydrogen evolution reaction. *J. Am. Chem. Soc.* **133**, 13363-13374 (2011).
16. Jiang, M., Zhu, D., Cai, J., Zhang, H. & Zhao, X. Electrocatalytic hydrogen evolution and oxygen reduction on polyoxotungstates/graphene nanocomposite multilayers. *J. Phys. Chem. C* **118**, 14371-14378 (2014).
17. Phuruangrat, A., Ham, D. J., Hong, S. J., Thongtema, S. & Lee, J. S. Synthesis of hexagonal WO_3 nanowires by microwave-assisted hydrothermal method and their electrocatalytic activities for hydrogen evolution reaction. *J. Mater. Chem.* **20**, 1683-1690 (2010).
18. Cheng, L., Huang, W., Gong, Q., Liu, C., Liu, Z., Li, Y. & Dai, H. Ultrathin WS_2 nanoflakes as a high-performance electrocatalyst for the hydrogen evolution reaction. *Angew. Chem. Int. Ed.* **53**, 7860 -7863 (2014).
19. Lukowski, M. A., Daniel, A. S., English, C. R., Meng, F., Forticaux, A., Hamers, R. J. & Jin, S. Highly active hydrogen evolution catalysis from metallic WS_2 nanosheets. *Energy Environ. Sci.* **7**, 2608-2613 (2014).
20. Peng, S., Li, L., Han, X., Sun, W., Srinivasan, M., Mhaisalkar, S. G., Cheng, F., Yan, Q., Chen, J. & Ramakrishna, S. Cobalt sulfide nanosheet/graphene/carbon nanotube nanocomposites as flexible electrodes for hydrogen evolution. *Angew. Chem. Int. Ed.* **53**, 12594-12599 (2014).
21. Huang, Z., Chen, Z., Chen, Z., Lv, C., Meng, H. & Zhang, C. $Ni_{12}P_5$ nanoparticles as an efficient catalyst for hydrogen generation via electrolysis and photoelectrolysis. *ACS Nano* **8**, 8121-8129 (2014).

22. Popczun, E. J., Read, C. G., Roske, C. W., Lewis, N. S. & Schaak, R. E. Highly active electrocatalysis of the hydrogen evolution reaction by cobalt phosphide nanoparticles. *Angew. Chem. Int. Ed.* **53**, 5427-5430 (2014).
23. Tian, J., Liu, Q., Asiri, A. M. & Sun, X. Self-supported nanoporous cobalt phosphide nanowire arrays: An efficient 3D hydrogen-evolving cathode over the wide range of pH 0–14. *J. Am. Chem. Soc.* **136**, 7587-7590 (2014).
24. Faber, M. S., Dziedzic, R., Lukowski, M. A., Kaiser, N. S., Ding, Q. & Jin, S. High-performance electrocatalysis using metallic cobalt pyrite (CoS_2) micro- and nanostructures. *J. Am. Chem. Soc.* **136**, 10053-10061 (2014).
25. Xu, K., Wang, F., Wang, Z., Zhan, X., Wang, Q., Cheng, Z., Safdar, M. & He, J. Component-controllable $WS_{2(1-x)}Se_{2x}$ nanotubes for efficient hydrogen evolution reaction. *ACS Nano* **8**, 8468-8476 (2014).
26. Zheng, X., Xu, J., Yan, K., Wang, H., Wang, Z. & Yang, S. Space-confined growth of MoS_2 nanosheets within graphite: The layered hybrid of MoS_2 and graphene as an active catalyst for hydrogen evolution reaction. *Chem. Mater.* **26**, 2344-2353 (2014).
27. Kong, D., Wang, H., Lu, Z. & Cui, Y. $CoSe_2$ nanoparticles grown on carbon fiber paper: an efficient and stable electrocatalyst for hydrogen evolution reaction. *J. Am. Chem. Soc.* **136**, 4897-4900 (2014).
28. Kibsgaard, J., Jaramillo, T. F. & Besenbacher, F. Building an appropriate active-site motif into a hydrogen-evolution catalyst with thiomolybdate $[Mo_3S_{13}]^{2-}$ clusters. *Nat. Chem.* **6**, 248-253 (2014).
29. Kibsgaard, J. & Jaramillo, T. F. Molybdenum phosphosulfide: an active, acid-stable, earth-abundant catalyst for the hydrogen evolution reaction. *Angew. Chem. Int. Ed.* **53**, 14433-14437 (2014).
30. Kibsgaard, J., Chen, Z., Reinecke, B. N. & Jaramillo, T. F. Engineering the surface structure of MoS_2 to preferentially expose active edge sites for electrocatalysis. *Nat. Mater.* **11**, 963-969 (2012).
31. Voiry, D., Yamaguchi, H., Li, J., Silva, R., Alves, D. C. B., Fujita, T., Chen, M., Asefa, T., Shenoy, V. B., Eda, G. & Chhowalla, M. Enhanced catalytic activity in strained chemically exfoliated WS_2 nanosheets for hydrogen evolution. *Nat. Mater.* **12**, 850-855 (2013).
32. Smith, A. J., Chang, Y.; Raidongia, K.; Chen, T.; Li, L. & Huang, J. Molybdenum sulfide supported on crumpled graphene balls for electrocatalytic hydrogen production. *Adv. Energy Mater.* **4**, DOI: 10.1002/aenm.201400398 (2014).
33. Qin, J-S., Du, D-Y., Guan, W., Bo, X-J., Li, Y-F., Guo, L-P., Su, Z-M., Wang, Y-Y., Lan, Y. Q. & Zhou,

H-C. Ultrastable polymolybdate-based metal−organic frameworks as highly active electrocatalysts for hydrogen generation from water. *J. Am. Chem. Soc.* **137**, 7169-7177 (2015).